Journal of Geodynamics 168 (2026) 102144

Contents lists available at ScienceDirect

Journal of Geodynamics

journal homepage: www.elsevier.com/locate/jog

Absolute ages of multiple deformation events in the eastern Sichuan Basin by U–Pb dating of slickenfiber calcite

Liang Luo [a,b,*], Lianbo Zeng [a,b], Yangfan Zhou [a,b], Xuan Yang [a,b]

[a] State Key Laboratory of Petroleum Resources and Engineering, China University of Petroleum (Beijing), Beijing 102249, China
[b] College of Geosciences, China University of Petroleum (Beijing), Beijing 102249, China

ARTICLE INFO

Keywords:
Calcite U-Pb dating
Eastern Sichuan Basin
Deformation event
Longmenshan
Tibetan Plateau

ABSTRACT

This study represents the pioneering application of calcite U–Pb dating to directly date multiple deformation events in the eastern Sichuan Basin, China. This approach is crucial for advancing our understanding of the Meso–Cenozoic tectonic evolution of the Yangtze Block and the Tibetan Plateau. We present calcite U–Pb dating results from three reverse/strike-slip faults, which allow us to constrain four distinct deformation events. The data reveal that the first deformation event along the approximately west–east–striking reverse fault occurred at the end of the Middle Jurassic (~164 Ma). This event is associated with northward subduction of the Bangong–Nujiang Ocean. Subsequent deformation event along the northeast-striking Qiyueshan Fault Zone occurred during the Early Cretaceous (~135 Ma) and is interpreted as resulting from far-field oblique flat-slab subduction of the Paleo-Pacific Plate. Reactivation of the Qiyueshan Fault Zone during the Eocene (~48 Ma) was driven by NW–SE compression associated with the thrusting of the Longmenshan fold–thrust belt, marking the first documented instance of this deformation event in the eastern Sichuan Basin. The youngest age, dating to the Oligocene (~28 Ma), is linked to a near north-south-striking strike-slip fault. This final deformation event is attributed to the eastern expansion of the Tibetan Plateau and the subsequent counterclockwise rotation of the Sichuan Basin.

1. Introduction

A defining tectonic feature of the South China Block—which comprises the western Yangtze Block and the eastern Cathaysia Block—is an approximately 1300-km-wide intracontinental fold-thrust belt (Li & Li, 2007). This belt is structurally partitioned into two distinct domains: a thick-skinned deformation zone in western Hunan and Hubei provinces, and a thin-skinned deformation zone that extends extending across the eastern Sichuan Basin (Fig. 1a and b). Especially, the eastern Sichuan Basin—renowned for its well-developed Jura-type fold belt and prolific hydrocarbon accumulations—has long constituted a pivotal natural laboratory for investigating intracontinental deformation processes. The prominent fold belt in the eastern Sichuan Basin has been shaped by multiple major tectonic events, resulting in the development of several structurally distinct deformation sets characterized by contrasting orientations (Fig. 1b). These events include the lateral extrusion and rotation of the Qinling–Dabie Orogen, the clockwise rotation of the Yangtze Block (Meng and Zhang, 2000; Faure et al., 2001), the Mesozoic collision involving the Lhasa, Qiangtang, and Indochina Blocks (Enkin et al., 1992), the subduction of the Pacific Plate (Northrup et al., 1995), and the Cenozoic uplift of the Tibetan Plateau (Yin, 2010). Previous thermochronology studies, primarily addressing northeast-trending structures, have produced conflicting results, with reported ages ranging from approximately 240–70 Ma, and even as recent as 19 Ma (Yan et al., 2003; Liu et al., 2015; Cao et al., 2023). Thermochronology such as apatite fission track dates record an exhumation age associated with cooling below ~100°C (Ault et al., 2019), they may not correspond to an age of fault activity but rather record an erosion process that is related to both climatic and tectonic processes (e.g., Champagnac et al., 2007; Bilau et al., 2021). Therefore, the precise timing and absolute ages of formation for these structures with distinct orientations remain unresolved structural issues.

The application of synkinematic calcite U–Pb dating to determine the timing of fault activity is an emerging field of study (Bilau et al., 2023b). This method has recently been applied in various regions, including the Central Alps (Ring and Gerdes, 2016), the Atlantic margin (Roberts and Walker, 2016), the Dead Sea transform (Nuriel et al., 2017), and the North Anatolian fault zone (Nuriel et al., 2019). Moreover, calcite U–Pb

* Corresponding author at: State Key Laboratory of Petroleum Resources and Engineering, China University of Petroleum (Beijing), Beijing 102249, China.
E-mail address: luoliang1225@163.com (L. Luo).

https://doi.org/10.1016/j.jog.2026.102144
Received 10 April 2025; Received in revised form 11 March 2026; Accepted 11 March 2026
Available online 14 March 2026
0264-3707/© 2026 Elsevier Ltd. All rights are reserved, including those for text and data mining, AI training, and similar technologies.

dating is increasingly being applied to bridge the gap between small scale deformation ages and plate-scale orogenic processes—commonly inferred from magmatic and metamorphic records (e.g., Amidon et al., 2022; Mouthereau et al., 2025). Such brittle deformation is documented even in far-field intraplate settings (Bilau et al., 2023b; Julien-Sicre et al., 2025). We employ calcite U–Pb geochronology to date a series of superimposed deformation events, which is crucial for advancing our understanding of the Meso–Cenozoic tectonic evolution and dynamic processes of the Yangtze Block and the Tibetan Plateau.

2. Geological background

The eastern Sichuan Basin, situated in the western region of the South China Block (Fig. 1a), has undergone a prolonged and intricate

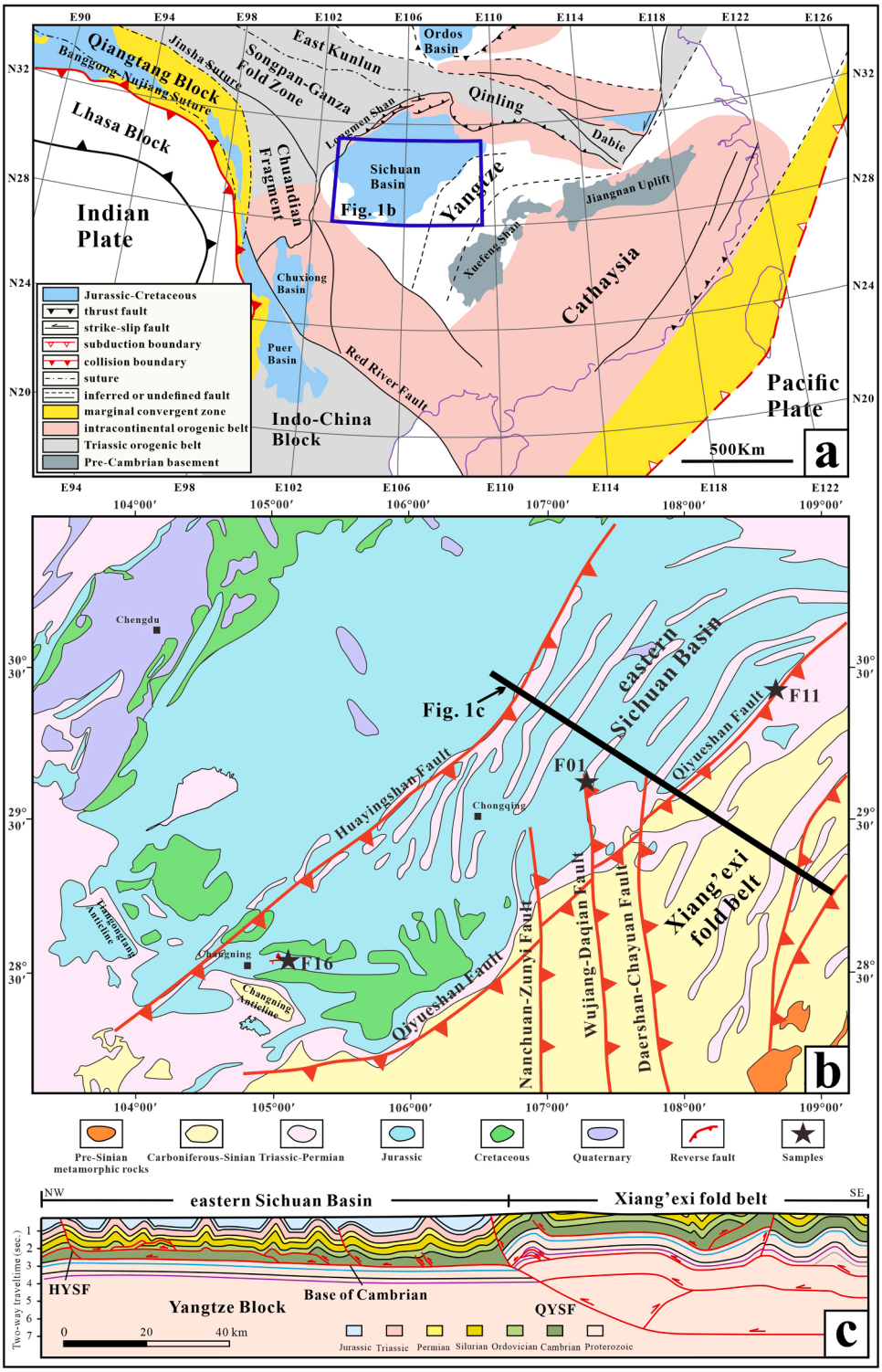

Fig. 1. (a) Simplified geological map of southern and western China, showing the distribution of Late Mesozoic contractional tectonic features (modified after Zhang et al. (2022)). (b) Simplified geological map of the eastern Sichuan Basin and its surrounding regions. (c) Geological cross-section across the thick-skinned Xiang'exi and the thin-skinned eastern Sichuan fold belts constructed from the interpreted SINOPROBE deep seismic reflection profiles (modified from Li et al. (2018)).

tectonic evolution. The structural deformation that began in the Yanshanian period (spanning the Jurassic and Cretaceous) has played a crucial role in shaping its present-day structural characteristics (Liu et al., 2015; He and Zhou, 2018; Qiu et al., 2020). During the Mesozoic, the Andean-type retro-arc foreland system shifted from the southeastern coastal area to the northwestern intracontinental thrust system within the Yangtze Block. This migration was driven by the flat-slab subduction of the Paleo–Pacific Plate (Li et al., 2014, 2018; Dong et al., 2015). The surface uplift and denudation in the eastern Sichuan Basin are believed to have commenced during the Cretaceous (Yan et al., 2003; Deng et al., 2013; Zhu et al., 2019; Li et al., 2020). Moreover, numerous studies have reported a subsequent period of rapid exhumation in the eastern Sichuan Basin during the Cenozoic (Li et al., 2015; Tian et al., 2018). Such results indicate that the eastern Sichuan Basin experienced fault reactivation in the Cenozoic, which is linked to regional surface uplift caused by the eastward growth of the Tibetan Plateau (Tapponnier, 2001; Royden et al., 2008).

Since the Neoproterozoic, the eastern Sichuan Basin has accumulated thousands of meters of both marine and terrestrial sedimentary layers. The stratigraphic sequence spanning from the Precambrian to the

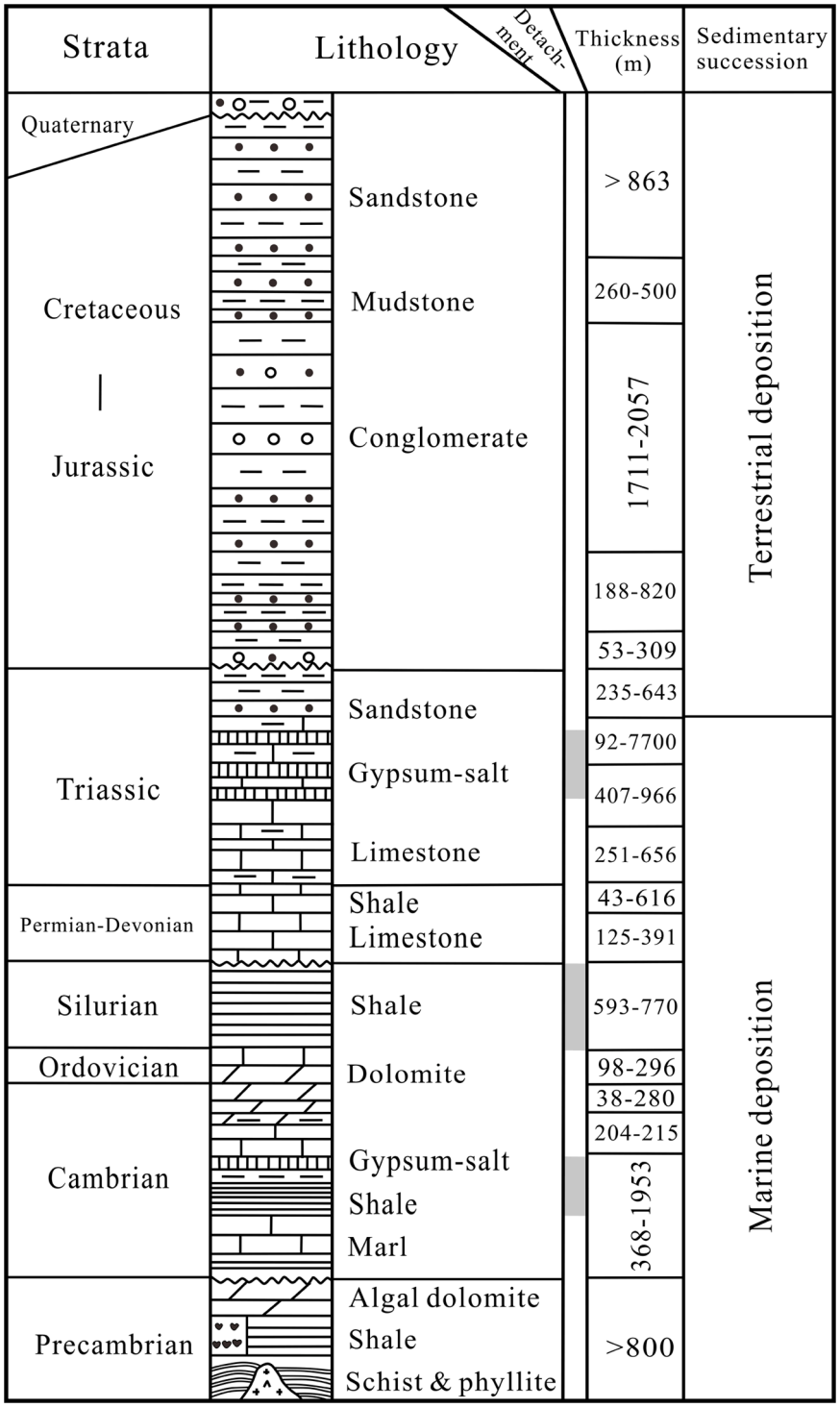

Fig. 2. Schematic stratigraphic column of the eastern Sichuan Basin (modified from Yan et al. (2003)).

Cretaceous includes two main depositional phases: (1) marine deposits ranging from the Precambrian to the Middle Triassic and (2) terrestrial deposits extending from the Upper Triassic to the Cretaceous (Fig. 2) (Yang et al., 2016; Feng et al., 2018; Gu et al., 2021). In the eastern Sichuan Basin, Cenozoic deposition has occurred to a relatively limited extent. The sedimentary sequence in the eastern Sichuan Basin comprises thick competent layers, which are interspersed by three main incompetent layers: the Cambrian evaporite, the Silurian shale, and the Lower–Middle Triassic evaporite (Yan et al., 2003; Li et al., 2015; Gu et al., 2021) (Fig. 2). These three principal decollements are widely recognized as key factors influencing the structural styles of the fold-and-thrust belt in the eastern Sichuan Basin (Yan et al., 2003; Wang et al., 2010; Li et al., 2015, 2021; Gu et al., 2021).

In the eastern Sichuan Basin, a thin-skinned thrust belt is characterized by narrow outcrops of Triassic strata with variable thicknesses forming the cores of anticlinal structures, while broader exposures of Cretaceous rocks constitute the cores of synclinal folds. This arrangement gives rise to a fold system where anticlines exhibit chevron shapes and synclines display box-like forms (Fig. 1b and c). The cross-sectional view reveals that several approximately symmetric thrust faults are closely associated with narrow anticlines and open synclines, all of which converge toward the Cambrian evaporite layer (Yan et al., 2003;

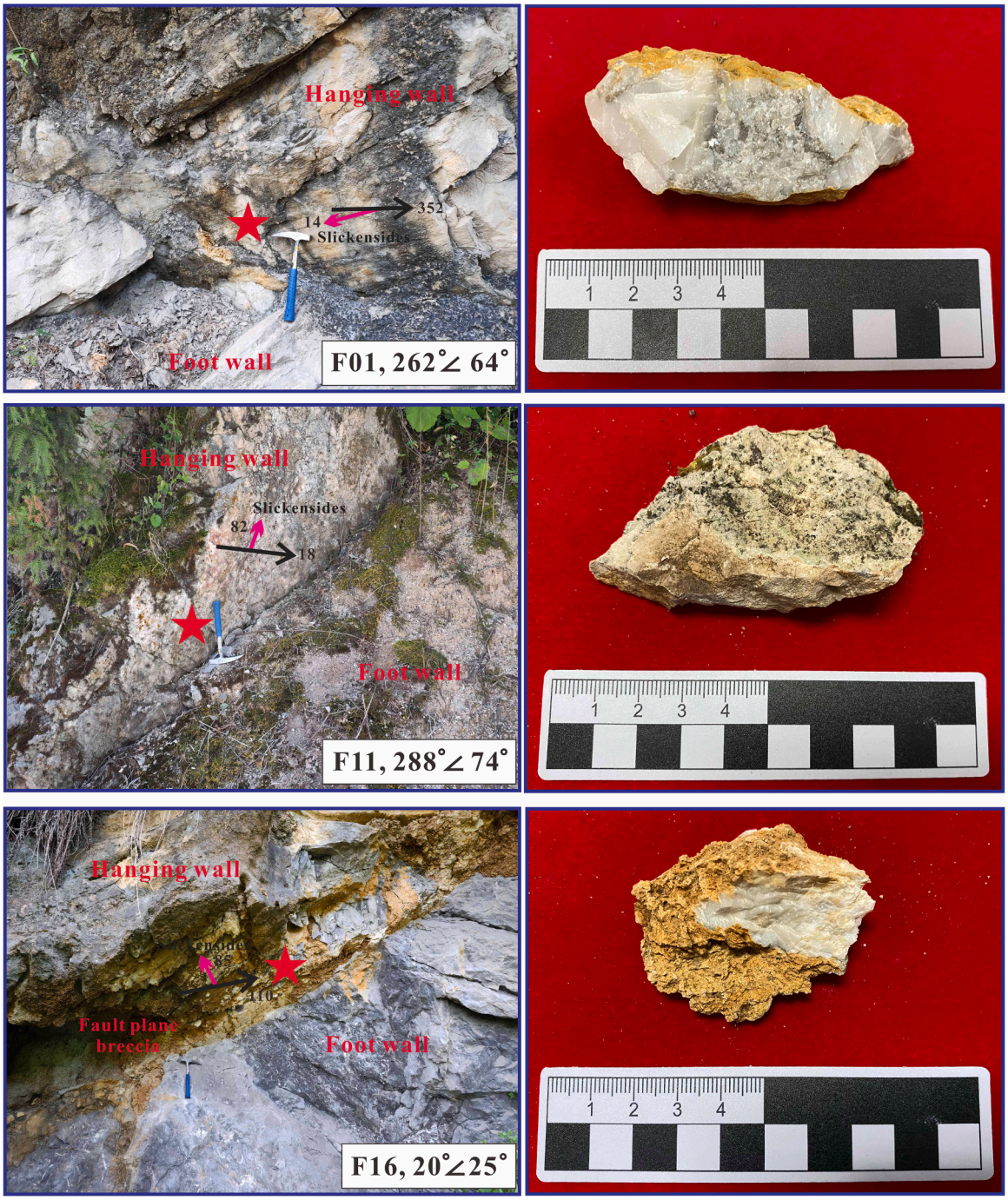

Fig. 3. Photographs of reverse/strike-slip faults and slickenfiber calcite samples from the eastern Sichuan Basin. The black line indicates the strike of the fault plane, and the associated number specifies its azimuth. The red line with arrow indicates the slip direction of the hanging wall, and the associated number denotes its pitch angle.

Gu et al., 2021; Xu et al., 2024) (Fig. 1c). The majority of the faulted detachment folds in the area dip toward the southeast and display greater displacement in the backthrusts. Thrust faults predominantly form along the limbs of anticlines. Within these anticlines, major forethrusts and backthrusts extend into the Triassic evaporites, while minor thrust faults connect adjacent detachment layers. The detachments, which are easily recognizable due to variations in thickness, define many of the thrust boundaries. Importantly, deformation below the Cambrian evaporites is minimal. Prominent unconformities between the Cretaceous strata and underlying units along these folds indicate that substantial deformation occurred during the Late Jurassic–Early Cretaceous interval (Hu et al., 2009; Mei et al., 2010).

The eastern Sichuan Basin exhibits an arcuate configuration in plane view (Fig. 1b). Structural orientations exhibit spatial variation: the axial traces trend approximately east–west in the northern part, northeast in the central part, and nearly north–south in the southern part. Additionally, several WNW–trending structures are present in the Changning shale gas field at the southern margin of the basin (Fig. 1b). Regions that have undergone multistage deformation exhibit intersecting sets of structures, thereby providing a relative chronology of the deformation events. Owing to the influence of the northeast–striking Huayingshan Fault, the trajectory of the WNW–trending Changning Anticline shifts westward and then turns southwestward (Fig. 1b). The Nanchuan–Zunyi, Wujiang–Daqian, and Daershan–Chayuan Faults, which strike approximately north–south, intersect the northeast–striking Qiyueshan Fault (Fig. 1b). Based on these superimposed deformation features, the sequence of structural development can be inferred as follows: WNW–trending structures formed initially, followed by NE–-trending structures, and ultimately nearly N–S–trending structures.

3. Samples and methods

Slickenfiber calcite is a valuable fault-related crystallization product, as it records syn-kinematic information on fault activity (Roberts and Holdsworth, 2022) and has been demonstrated to preserve successive deformation increments without resetting the U–Pb isotopic system (Bilau et al., 2023a). Ten calcite samples were collected from slickenfibers along ten reverse/strike-slip fault planes oriented with strikes of WNW, NE, and approximately N–S in the eastern Sichuan Basin (Figs. 1b and 3). Most of the fault planes exhibit polished surfaces (Fig. 3).

The calcite samples were initially embedded in epoxy resin and polished for Cathodoluminescence (CL) imaging to identify homogeneous areas suitable for U–Pb dating. Laser Ablation-Inductively Coupled Plasma Mass Spectrometry (LA–ICP–MS) in situ U–Pb dating was conducted at Guizhou Tongwei Analytical Technology Co., Ltd. The samples were cut, polished, and prepared into standard 2.5-cm-diameter mounts. These mounts were placed in a Laurin Technic sample holder for the analysis of ^{206}Pb, ^{207}Pb, ^{208}Pb, ^{238}U, and ^{232}Th ion beams using a RESOlution SE-S155 laser ablation system coupled with a Thermo iCap-RQ quadrupole ICP–MS. The laser was operated at a repetition rate of 15.21 Hz and a fluence of 6.0 J/cm^2, with a spot diameter of 120 μm. The analysis involved 15 s of background acquisition followed by 20 s of sample ablation. Prior to analysis, each spot was preablated with eight laser pulses to remove surface contamination. NIST614 was employed to correct the ratios of ^{206}Pb, ^{207}Pb, ^{208}Pb, ^{238}U, and ^{232}Th in the original data. Standard AHX-1d (with a recommended age of 238.2 ± 2.4 Ma) was utilized to calibrate the $^{238}U/^{206}Pb$ ratio and its deviations during testing, ensuring that the relative error of the measurements did not exceed 0.5%. The NIST series glass reference material, developed by the National Institute of Standards and Technology in the United States, contains fixed main elements including SiO_2 (~70%), Al_2O_3 (~2%), Na_2O (~13.5%), and CaO (~12%), along with 66 fixed trace elements, with a concentration of 1 μg/g for each element in NIST614 (Wu et al., 2015). The measured data for the laboratory standard sample PTKD-2 (with a recommended age of 153.7 ± 1.7 Ma) was 156.6 ± 3.6 Ma, which was consistent with the recommended value. Raw data were processed using Iolite software v3.6 to calculate the concentration of each element (ppm) (Paton et al., 2011). U–Pb data on three samples are presented in Table 1.

4. Results

CL images reveal that most slickenfiber calcite crystals are homogeneous, exhibiting medium-to-high bright orange luminescence. In contrast, the calcite crystal from sample F11 is heterogeneous, with a small portion displaying medium bright orange luminescence, while the remainder exhibits darker luminescence (Fig. 4).

The analytical results were plotted on Tera–Wasserburg concordia diagrams, and the ages were calculated as lower isochron intercepts using Isoplot v3.75 (Ludwig, 2012). Three slickenfiber calcite samples yielded meaningful isochrones, whereas the remaining samples exhibited extremely low U content and limited $^{238}U/^{206}Pb$ ratios or significant spread, rendering them unsuitable for dating. Sample F01 was collected from an approximately north–south–striking fault plane dipping to the west–southwest at 64° (Fig. 3). Striations and slickenside lineations on this fault plane indicate predominantly left-lateral strike-slip motion. Calcite U–Pb dating of sample F01 yields an age of 27.8 ± 4.8 Ma (n = 27, MSWD = 1.1) (Fig. 5; Table 2). Sample F11 was collected from a northeast–striking fault plane dipping 74° to the west–northwest (Fig. 3). This fault represents a structurally coherent segment of the Qiyueshan Fault Zone. Kinematic analysis of striations and slickenside lineations on the fault surface indicates dominantly reverse-sense slip, which was the result of northwest–southeast–directed compressive stress. Calcite U–Pb dating reveals two distinct ages: 47.6 ± 5.6 Ma (F11-a, n = 37, MSWD = 0.51) and 135.4 ± 8.1 Ma (F11-b, n = 58, MSWD = 1.7), interpreted as recording two discrete deformation events (Fig. 5; Table 2). Additionally, sample F16 was collected from a nearly west–east–striking fault plane dipping 25° to the north–northeast (Fig. 3). Kinematic analysis of striations and slickenside lineations on this surface indicates dominantly reverse-sense slip, which was the result of approximately north–south–directed compressive stress. Calcite U–Pb dating yields an age of 163.6 ± 11.3 Ma (n = 41, MSWD = 0.3) (Fig. 5; Table 2).

5. Discussion

This study represents the inaugural application of LA–ICP–MS U–Pb dating to slickenfiber calcite for directly dating multiple deformation events in the eastern Sichuan Basin. It successfully provides precise chronological constraints on four distinct deformation events, spanning from the Middle Jurassic to the Oligocene.

5.1. Deformation event 1

During the Mesozoic, a major tectonic event in western China was the subduction of the Meso-Tethys Ocean, which eventually led to the collision between the Lhasa and Qiangtang Blocks (Figs. 1a and 6). Zircon U–Pb dating indicates two separate magmatic phases: the Early–Middle Jurassic (187–171 Ma) and the Middle–Late Jurassic (169–147 Ma) (Zhong et al., 2018; Liu et al., 2019), both associated with the northern subduction of the Bangong–Nujiang Ocean. Additionally, phengite discovered in the Jiayuqiao Metamorphic Complex shows a $^{40}Ar/^{39}Ar$ age of 167 Ma, offering evidence of high-pressure shearing deformation during the Middle Jurassic in the southwestern Bangong–Nujiang Suture (Wang et al., 2008).

We propose that the first deformation event–constrained to the Middle Jurassic (~164 Ma) by calcite U–Pb geochronology of sample F16–generated west–east–striking reverse faults along the southern margin of the eastern Sichuan Basin, in response to far-field north–south–directed compressive stress induced by northward subduction of the Bangong–Nujiang Ocean (Fig. 6).

Table 1
U-Pb isotope data of slickenfibre calcite samples in the eastern Sichuan Basin.

Spot	Sample ID	^{206}Pb (cps)	U (PPM)	Pb (PPM)	Th/U	^{238}U/^{206}Pb	±2σ	^{207}Pb/^{206}Pb	±2σ
F01									
F01_1	F01	86	0.00111	0.00272	0.386	0.795936	0.074619	0.905	0.02
F01_2	F01	100	0.02102	0.00317	1.006	23.1545	1.56368	0.85	0.065
F01_3	F01	101	0.0317	0.00297	0.384	18.7279	1.9082	0.84	0.07
F01_4	F01	126	0.00153	0.00373	0.322	0.891448	0.160461	0.94	0.02
F01_7	F01	118	0.0291	0.00378	2.505	25.76439	0.893563	0.882	0.038
F01_9	F01	92	0.00344	0.00315	0.203	4.265302	0.336734	0.95	0.11
F01_10	F01	126	0.00084	0.00414	1.686	0.474175	0.051705	0.92	0.06
F01_11	F01	366	0.119	0.0107	0.539	31.95154	1.660564	0.806	0.037
F01_12	F01	120	0.0201	0.00348	1.569	17.07755	1.34134	0.96	0.075
F01_13	F01	104	0.00081	0.00364	12.308	0.761921	0.052097	0.99	0.065
F01_15	F01	61.5	0.00321	0.00231	0.567	4.871301	0.732026	0.91	0.1
F01_16	F01	409	0.1967	0.01173	0.038	52.28435	1.364606	0.79	0.03
F01_17	F01	409	0.1967	0.01173	0.038	55.28435	0.864606	0.75	0.03
F01_19	F01	128	0.0503	0.00373	17.828	41.85203	2.259616	0.719	0.048
F01_22	F01	660	0.141	0.0196	4.010	23.83551	1.24276	0.77	0.055
F01 _25	F01	108	0.0201	0.0037	3.678	19.5493	1.136089	0.92	0.065
F01_28	F01	171	0.0339	0.0052	1.010	21.7958	1.17239	0.9	0.055
F01_29	F01	261	0.1214	0.00758	0.678	60.09102	1.003116	0.694	0.027
F01_32	F01	249	0.0131	0.00833	0.238	1.255561	0.282944	1.02	0.065
F01_34	F01	347	0.01657	0.0117	0.147	4.898066	0.269124	0.975	0.049
F01_35	F01	145	0.0087	0.00505	1.012	3.106091	0.303033	1.05	0.055
F01_38	F01	118	0.0291	0.00378	2.505	24.29014	1.720827	0.83	0.06
F01_41	F01	98	0.01071	0.00317	7.666	11.1431	0.766088	0.92	0.08
F01_42	F01	196	0.0586	0.00618	4.239	30.21858	1.536538	0.782	0.048
F01_45	F01	325	0.1138	0.00974	4.220	36.09102	1.388116	0.774	0.027
F01_48	F01	61.5	0.0067	0.00216	19.815	11.42882	0.952402	0.81	0.06
F01_51	F01	84	0.0069	0.00239	0.251	8.33129	0.6229	0.83	0.07
F11-a									
F11-a_1	F11-a	36300	0.663	0.687	0.143	2.950652	0.068294	0.3227	0.0056
F11-a_4	F11-a	37700	0.682	0.739	0.032	1.808212	0.095362	0.3507	0.0059
F11-a_5	F11-a	49500	0.971	0.993	0.038	2.142904	0.061815	0.3745	0.0038
F11-a_7	F11-a	42300	0.989	0.84	0.051	2.396366	0.090186	0.3497	0.006
F11-a_9	F11-a	31700	1.21	0.619	0.099	3.594549	0.188424	0.3402	0.0057
F11-a_10	F11-a	30800	0.816	0.601	0.068	12.88681	0.093485	0.272	0.011
F11-a_11	F11-a	42200	0.809	0.839	0.047	11.99876	0.071704	0.292	0.013
F11-a_13	F11-a	30200	0.609	0.555	0.071	7.251132	0.108009	0.324	0.0049
F11-a_14	F11-a	32100	0.51	0.614	0.049	1.681977	0.076165	0.3331	0.0074
F11-a_15	F11-a	49000	1.202	1.01	0.046	4.083908	0.134813	0.332	0.0068
F11-a_16	F11-a	57300	0.881	1.205	0.034	1.550344	0.078191	0.3614	0.006
F11-a_17	F11-a	35100	2.11	0.66	0.095	6.05046	0.374123	0.3195	0.0039
F11-a_18	F11-a	70100	1.279	1.5	0.053	1.80455	0.131506	0.35	0.007
F11-a_20	F11-a	58000	0.952	1.25	0.050	10.72427	0.156752	0.289	0.0092
F11-a_21	F11-a	37300	0.627	0.708	0.086	1.797274	0.079718	0.3597	0.0077
F11-a_22	F11-a	59300	1.383	1.24	0.045	8.614217	0.137994	0.3011	0.0059
F11-a_23	F11-a	30500	0.659	0.575	0.030	12.01685	0.109512	0.283	0.0062
F11-a_25	F11-a	41660	1.83	0.855	0.091	4.244991	0.242571	0.329	0.0083
F11-a_27	F11-a	41600	0.839	0.856	0.047	12.2472	0.084297	0.275	0.0064
F11-a_29	F11-a	33400	0.611	0.641	0.051	8.826738	0.123529	0.3154	0.0055
F11-a_30	F11-a	24850	0.391	0.429	0.036	8.830489	0.71415	0.2936	0.0045
F11-a_33	F11-a	51400	1.02	1.13	0.049	8.168973	0.200538	0.303	0.01
F11-a_36	F11-a	32400	0.717	0.635	0.071	2.256831	0.097129	0.3288	0.007
F11-a_37	F11-a	34700	0.96	0.682	0.084	3.810366	0.088599	0.3244	0.0065
F11-a_38	F11-a	34400	0.602	0.685	0.049	1.808212	0.091694	0.3368	0.0047
F11-a_39	F11-a	28700	0.793	0.549	0.105	8.803296	0.158677	0.3062	0.0046
F11-a_41	F11-a	28300	0.592	0.536	0.045	11.06833	0.124771	0.291	0.011
F11-a_43	F11-a	38200	1.018	0.751	0.063	2.812139	0.106453	0.329	0.0049
F11-a_44	F11-a	41400	0.816	0.827	0.038	2.038062	0.055914	0.3444	0.0069
F11-a_45	F11-a	44700	2.13	0.892	0.076	13.85908	0.400944	0.2696	0.0079
F11-a_46	F11-a	30400	0.979	0.6	0.060	3.289476	0.157798	0.3315	0.0065
F11-a_47	F11-a	25600	0.998	0.478	0.041	3.277383	0.313279	0.347	0.0054
F11-a_48	F11-a	32900	0.872	0.625	0.049	8.794508	0.122643	0.3104	0.0034
F11-a_49	F11-a	41600	1.23	0.82	0.409	5.409319	0.209504	0.3278	0.0056
F11-a_52	F11-a	43700	0.602	0.952	0.027	7.424038	0.084168	0.3096	0.0075
F11-a_53	F11-a	48900	0.722	0.99	0.032	1.513494	0.107923	0.354	0.005
F11-a_54	F11-a	32500	1.71	0.662	0.061	10.01553	0.27132	0.2937	0.0078
F11-a_55	F11-a	56000	1.43	1.22	0.063	11.981	0.2817416	0.2791	0.0098
F11-a_56	F11-a	45600	0.663	0.927	0.048	8.495718	0.050192	0.3062	0.0067
F11-a_58	F11-a	19500	1.06	0.345	0.154	5.194919	0.284570	0.3271	0.003
F11-a_60	F11-a	43700	1.004	0.888	0.071	2.082823	0.136259	0.3639	0.0081
F11-a_62	F11-a	36600	1.16	0.729	0.086	2.903740	0.170252	0.3499	0.0061
F11-a_64	F11-a	74400	1.19	1.61	0.084	7.534334	0.087148	0.3088	0.0058
F11-a_67	F11-a	42500	0.761	0.9	0.055	1.904803	0.113963	0.3731	0.0084

(*continued on next page*)

Table 1 (*continued*)

Spot	Sample ID	^{206}Pb (cps)	U (PPM)	Pb (PPM)	Th/U	$^{238}U/^{206}Pb$	±2σ	$^{207}Pb/^{206}Pb$	±2σ
F11-a_68	F11-a	36800	0.619	0.747	0.044	1.761755	0.094007	0.3503	0.0049
F11-a_71	F11-a	28600	0.771	0.576	0.053	2.742917	0.151915	0.333	0.0074
F11-a_72	F11-a	25800	1.3	0.491	0.138	4.686899	0.202064	0.3285	0.0054
F11-a_73	F11-a	51400	1.19	1.09	0.065	13.3772	0.088749	0.2693	0.0048
F11-a_74	F11-a	30700	0.391	0.6	0.037	1.414997	0.069627	0.352	0.01
F11-a_75	F11-a	29000	0.672	0.567	0.045	8.469385	0.136808	0.3081	0.0081
F11-a_76	F11-a	47900	1.27	1.01	0.040	1.819282	0.252472	0.363	0.0081
F11-a_77	F11-a	39100	0.761	0.809	0.032	1.888661	0.104036	0.3602	0.0084
F11-a_78	F11-a	39900	0.834	0.818	0.070	2.112436	0.080092	0.3452	0.005
F11-a_79	F11-a	33600	0.96	0.702	0.052	2.645246	0.266879	0.346	0.011
F11-a_80	F11-a	29300	0.4	0.605	0.031	1.414997	0.062889	0.3499	0.0081
F11-a_82	F11-a	23700	0.647	0.414	0.030	7.967877	0.06905	0.298	0.0049
F11-a_83	F11-a	47900	2.23	0.981	0.094	7.937931	0.07162	0.3049	0.0042
F11-a_84	F11-a	44200	1.63	0.866	0.046	7.087132	0.198866	0.321	0.01
F11-b									
F11-b_1	F11-b	31700	1.7	0.696	0.593	4.4350648	0.30891	0.3935	0.01
F11-b_4	F11-b	39500	1.72	0.891	0.176	4.185203	0.255435	0.4118	0.0078
F11-b_7	F11-b	43100	4.19	0.912	0.273	9.60612	0.393354	0.3704	0.0073
F11-b_9	F11-b	48200	3.35	1.098	0.375	5.469006	0.369074	0.4138	0.0072
F11-b_10	F11-b	49800	6.28	1.09	0.378	12.178251	0.648841	0.386	0.0042
F11-b_11	F11-b	50600	2.2	1.124	0.351	3.761384	0.206321	0.3903	0.0078
F11-b_13	F11-b	57100	5.14	1.274	0.613	8.261799	0.535983	0.3993	0.0051
F11-b_16	F11-b	45800	3.63	1.049	0.381	7.959358	0.262943	0.4038	0.0086
F11-b_17	F11-b	41200	2.64	0.929	0.407	6.632798	0.296107	0.3958	0.0064
F11-b_21	F11-b	51000	1.86	1.15	0.220	2.951815	0.400743	0.41	0.011
F11-b_24	F11-b	36000	2.356	0.813	0.220	6.304442	0.374521	0.396	0.0067
F11-b_25	F11-b	59700	2.94	1.4	0.328	2.409319	0.397212	0.414	0.013
F11-b_28	F11-b	45600	3.78	1.015	0.396	8.163444	0.351357	0.3953	0.0078
F11-b_30	F11-b	27840	4.41	0.59	0.305	14.54238	0.735422	0.3575	0.0046
F11-b_31	F11-b	44100	1.45	1.01	0.162	2.839006	0.171787	0.4157	0.0097
F11-b_32	F11-b	38600	1.606	0.9	0.198	4.0155324	0.379848	0.409	0.014
F11-b_36	F11-b	43000	3.35	0.948	0.372	7.826585	0.508488	0.3757	0.0095
F11-b_37	F11-b	50800	4.86	1.12	0.417	8.170927	0.501789	0.3884	0.0061
F11-b_41	F11-b	35100	4.32	0.785	0.451	11.50256	0.697574	0.3913	0.0091
F11-b_44	F11-b	38000	2.096	0.89	0.356	5.2131465	0.335349	0.4246	0.0056
F11-b_48	F11-b	55700	1.9	1.302	0.336	2.922781	0.201241	0.417	0.0068
F11-b_51	F11-b	74500	5.778	1.676	0.075	28.80692	1.82514	0.3301	0.013
F11-b_53	F11-b	31300	2.95	0.668	0.653	27.59978	0.738592	0.3345	0.009
F11-b_55	F11-b	29920	2.8	0.673	0.352	15.93103	1.01365	0.3723	0.02
F11-b_6	F11-b	37000	1.84	0.79	0.233	4.470652	0.224205	0.361	0.0069
F11-b_60	F11-b	39600	2.15	0.94	0.385	5.182837	0.512257	0.405	0.01
F11-b_65	F11-b	49000	2.12	1.131	0.164	3.859082	0.200472	0.4098	0.0063
F11-b_66	F11-b	33400	4.3	0.72	0.393	33.81749	1.67454	0.3225	0.011
F11-b_69	F11-b	61700	1.786	1.53	0.190	29.30695	0.67701	0.3239	0.017
F11-b_73	F11-b	40100	5.35	0.872	0.656	32.8713	0.63886	0.318	0.024
F11-b_77	F11-b	72000	7.43	1.71	0.260	33.36955	0.279272	0.324	0.0096
F11-b_62	F11-b	41400	6.51	0.946	0.304	14.83275	0.691043	0.3967	0.0094
F11-b_78	F11-b	93000	3.87	2.33	0.178	4.327418	0.525172	0.395	0.015
F11-b_84	F11-b	40700	2.11	0.951	0.330	4.908855	0.186515	0.4193	0.0073
F11-b_79	F11-b	51900	32.3	1.122	0.393	40.54238	1.47084	0.305	0.0092
F11-b_81	F11-b	24500	1.59	0.531	0.269	35.538	0.70844	0.328	0.0092
F11-b_51	F11-b	40900	8.22	0.927	0.451	18.8069248	0.912572	0.3801	0.0065
F16									
F16_1	F16	2940	0.05509	0.0752	0.228	1.8767327	0.067167279	0.514	0.014
F16_2	F16	4850	0.142	0.1204	0.224	12.88495	0.177391	0.371	0.011
F16_4	F16	1604	0.01713	0.04074	0.952	1.028199	0.048623	0.516	0.021
F16_6	F16	2950	0.0674	0.0751	0.931	2.261984	0.063136	0.501	0.016
F16_8	F16	2624	0.0671	0.0664	1.009	2.504068	0.084407	0.502	0.015
F16_10	F16	3110	0.0329	0.0806	0.076	0.922824	0.066871	0.511	0.016
F16_11	F16	2446	0.0465	0.0625	0.662	1.797274	0.101459	0.511	0.018
F16_12	F16	3377	0.0418	0.0857	0.244	1.214507	0.039711	0.501	0.013
F16_13	F16	2240	0.0448	0.0582	0.485	1.980996	0.066033	0.52	0.016
F16_14	F16	2713	0.05528	0.0689	0.820	2.03527	0.060408	0.498	0.016
F16_16	F16	3372	0.0935	0.0851	0.113	2.693197	0.097639	0.504	0.012
F16_20	F16	1310	0.01086	0.03391	0.478	0.800223	0.040227	0.522	0.022
F16_22	F16	2617	0.0442	0.0682	0.312	1.688348	0.047964	0.52	0.015
F16_24	F16	1731	0.01138	0.0453	0.182	0.631785	0.037164	0.535	0.02
F16_25	F16	7780	0.679	0.208	0.101	7.751722	0.548126	0.431	0.009
F16_27	F16	1640	0.02329	0.04218	0.638	1.403855	0.050848	0.519	0.019
F16_28	F16	2003	0.02534	0.0506	0.464	1.245039	0.045211	0.511	0.017
F16_29	F16	2420	0.0384	0.062	1.223	11.458998	0.095515	0.3905	0.014
F16_31	F16	2347	0.0244	0.0599	0.386	9.423337	0.249031	0.421	0.013
F16_32	F16	3504	0.0794	0.0876	0.349	2.229735	0.061348	0.496	0.012
F16_34	F16	2469	0.0604	0.0631	0.590	2.445674	0.066426	0.511	0.015
F16_35	F16	2871	0.0602	0.0718	0.391	12.07942	0.058206	0.386	0.012

(*continued on next page*)

Table 1 (*continued*)

Spot	Sample ID	^{206}Pb (cps)	U (PPM)	Pb (PPM)	Th/U	$^{238}U/^{206}Pb$	±2σ	$^{207}Pb/^{206}Pb$	±2σ
F16_38	F16	1978	0.0386	0.0506	1.745	1.888661	0.072025	0.512	0.016
F16_45	F16	3497	0.1011	0.0881	0.435	2.887749	0.077643	0.502	0.011
F16_50	F16	4185	0.1363	0.1055	0.074	3.179202	0.100909	0.492	0.013
F16_64	F16	2194	0.0615	0.0571	0.054	2.746297	0.093066	0.512	0.016
F16_67	F16	2681	0.00616	0.0705	0.227	12.21533	0.010922	0.381	0.013
F16_72	F16	3019	0.0608	0.0764	0.135	6.912979	0.061577	0.451	0.012
F16_74	F16	2418	0.01902	0.06583	0.409	0.759973	0.03693	0.54	0.016
F16_75	F16	2750	0.0651	0.0735	0.261	1.714323	0.158245	0.519	0.015
F16_76	F16	4810	0.1106	0.1288	0.155	2.107442	0.079714	0.521	0.012
F16_78	F16	6080	0.0705	0.1648	0.097	1.096492	0.049902	0.5318	0.01
F16_79	F16	3743	0.1443	0.1005	0.218	3.551586	0.183947	0.513	0.012
F16_80	F16	2008	0.00772	0.0561	0.049	10.34959	0.020564	0.405	0.01
F16_81	F16	2333	0.1937	0.0601	0.360	8.551586	0.367894	0.43	0.012
F16_82	F16	3521	0.265	0.0915	0.182	6.217825	0.221536	0.45	0.01
F16_83	F16	3990	0.2053	0.1067	0.211	4.533801	0.151143	0.475	0.004
F16_84	F16	1582	0.0985	0.04148	0.227	13.44568	0.258812	0.373	0.017
F16_86	F16	2964	0.2784	0.0746	0.716	8.074711	0.270624	0.439	0.015
F16_87	F16	2576	0.3544	0.071	0.250	10.0003	0.254192	0.417	0.009
F16_89	F16	2333	0.1937	0.0601	0.360	12.33513	0.120158	0.382	0.012

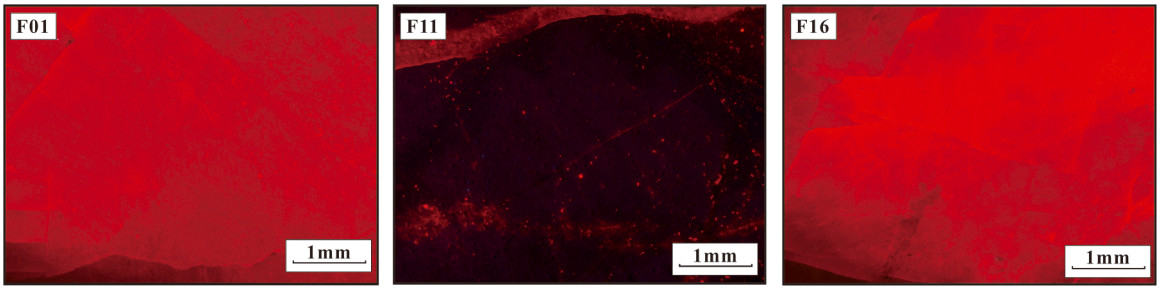

Fig. 4. CL images of slickenfiber calcite samples from the eastern Sichuan Basin.

5.2. Deformation event 2

The geographical pattern of apatite/zircon fission-track ages demonstrates a progressive reduction from the southeast to the northwest. This trend aligns with the idea of an extended and stable cooling and exhumation process, extending from the Xuefengshan fold belt, through the Xiang'exi fold belt, and eventually reaching the eastern Sichuan Basin (Shen et al., 2009; Mei et al., 2010; Shi et al., 2016). The northeast-striking Qiyueshan Fault extends into both the Wushan fault–fold belt in the north and the Daloushan fault–fold belt in the south, effectively delineating the present boundary between the Xiang'exi fold belt and the eastern Sichuan Basin (Fig. 1b). Significantly, apatite fission-track thermal modeling indicates that the onset of cooling took place during the Late Jurassic to Early Cretaceous (160–120 Ma) and mainly occurred after the Late Cretaceous (100–80 Ma) to the east and west of the Qiyueshan Fault, respectively (Mei et al., 2010; Li et al., 2020).

The second deformation event–constrained to the Early Cretaceous (~135 Ma) by calcite U–Pb geochronology of sample F16–is attributed to southeast–northwest–directed compressive stress originating from the Xuefengshan and Xiang'exi fold belts (Fig. 6). This compression may have been induced by far-field oblique flat-slab subduction of the Paleo-Pacific Plate (Li and Li, 2007; Shi et al., 2016; Dilek and Tang, 2021; Feng et al., 2023). Notably, this deformation event also impacted the Huayingshan Fault, which experienced deformation between 105 and 78 Ma (Cao et al., 2023).

5.3. Deformation event 3

In the piedmont area, the residual strata of the Upper Cretaceous Jiaguan Formation and the Eocene Lushan Formation exhibit an impressive thickness of exceeding 3400 m. In these strata, multiple sets of purplish–red conglomerate intervals gradually thin toward the southeast, forming wedge-shaped molasse deposits—a characteristic feature of the western Sichuan foreland basin. Additionally, a low-temperature thermochronology analysis reveals that the southern Longmenshan area underwent rapid uplift starting in the Late Cretaceous and persisting through the Paleogene (~70–40 Ma) (Jia et al., 2020).

We attribute the third deformation event–constrained to the Eocene (~48 Ma) by calcite U–Pb geochronology of sample F16–to the renewed thrusting of the Longmenshan fold–thrust belt. This event reactivated northeast-striking faults in the eastern Sichuan Basin, most prominently represented by the Qiyueshan Fault Zone (Fig. 6). To our knowledge, this represents the first well-constrained documentation of Eocene-aged thrust reactivation in the eastern Sichuan Basin.

5.4. Deformation event 4

No Oligocene-age deformation events have been identified in association with the Xuefengshan fold belt. Consequently, considering the tectonic background of that time, the final deformation event–constrained to the Oligocene (~28 Ma) by calcite U–Pb geochronology of sample F01–is believed to be linked to the early phase of eastern growth and extrusion of the Tibetan Plateau. Multiscale seismic tomography indicates that the structure of the Indian mantle lithosphere beneath the eastern Tibetan Plateau indicate that the Indian mantle lithosphere approached the thick Yangtze lithosphere initiated at 40–35 Ma (Hou et al., 2024). This collision precipitated the tearing of the Indian mantle lithosphere and simultaneously drove significant peripheral deformation of the Yangtze Craton. Notably, Cenozoic deformation in the eastern Sichuan Basin occurred with a discernible temporal lag relative to its

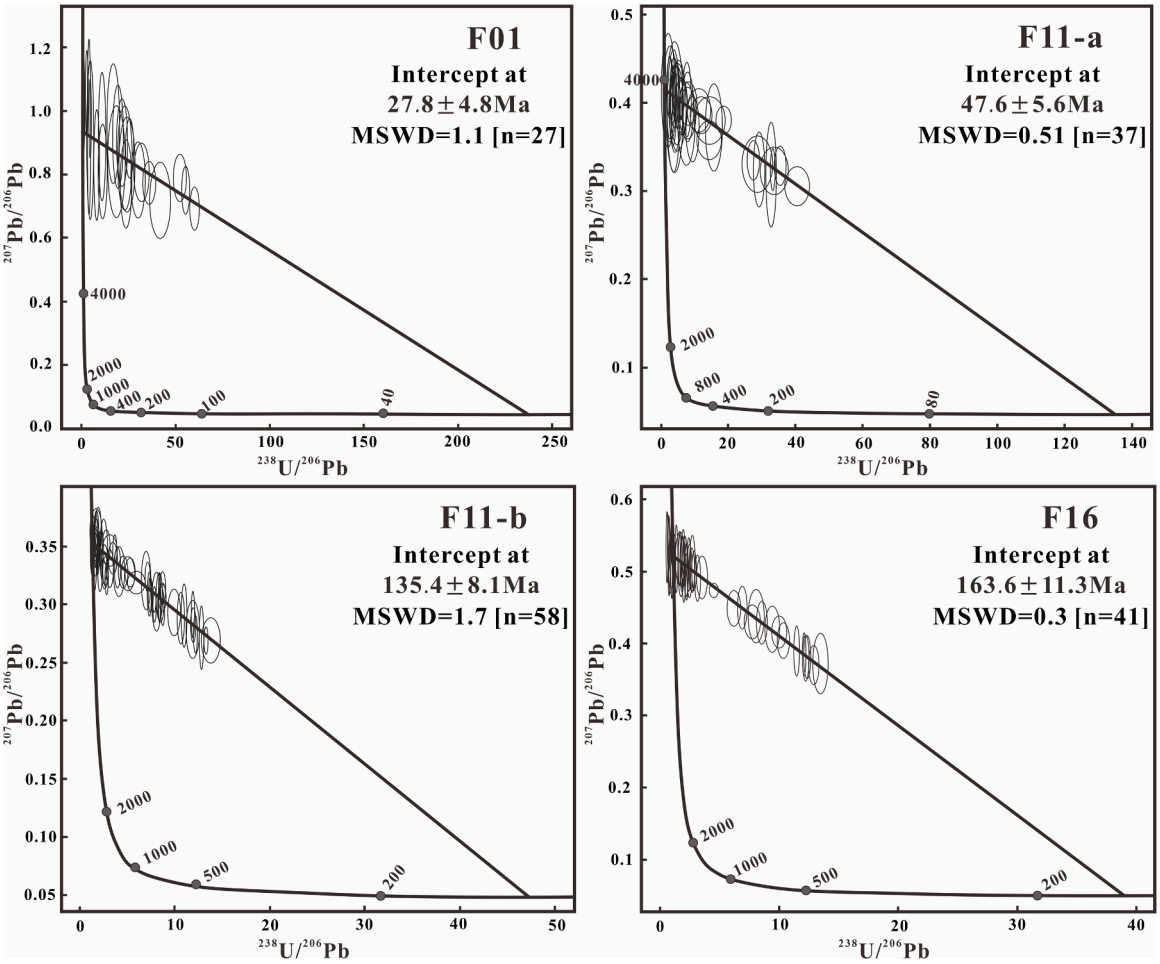

Fig. 5. Concordia plot of U-Pb dating results for slickenfiber calcite samples from the eastern Sichuan Basin. U-Pb data are plotted with 2σ error ellipses; age, uncertainties (2σ), mean square weighted deviation (MSWD), and number of spots are provided for each sample.

Table 2
Sample details and slickenfibre calcite U-Pb ages in the eastern Sichuan Basin.

Sample	Location	Structure	Event	Age (Ma)	±2σ	MSWD	Number of spots
F01	29.5550°N 107.3775°E	Strike-slip fault slickenfiber	4	27.8	4.8	1.1	27
F11-a	30.2417°N	Reverse fault	3	47.6	5.6	0.51	37
F11-b	108.6089°E	slickenfiber	2	135.4	8.1	1.7	58
F16	28.3747°N 105.1106°E	Reverse fault slickenfiber	1	163.6	11.3	0.3	41

western margin. Based on low-temperature thermochronological data, Tian et al. (2018) documented a pronounced episode of accelerated cooling between approximately 35 and 28 Ma in the eastern Sichuan Basin. This deformation event might also be contributed to the subsequent counterclockwise rotation of the Sichuan Basin. Wang et al. (2014) emphasized that Cenozoic deformation extended beyond the western margin of the Sichuan Basin, substantially affecting several other margins of the basin as well. Specifically, the eastern margin of the Sichuan Basin experienced NE–SW right-lateral shear (Fig. 6). This tectonic activity subsequently resulted in the development of near north–south–striking faults in the eastern Sichuan Basin (Fig. 6). Notably, these north–south–striking faults intersected the pre-existing northeast-striking Qiyueshan Fault (Fig. 1b), thereby forming a complex fault network.

6. Conclusions

Our findings demonstrate the successful application of U–Pb dating of slickenfiber calcite to constrain a complex sequence of deformation events in the superimposed deformation basin. Specifically, this study identifies four distinct deformation events in the eastern Sichuan Basin. The first deformation event, occurring at the end of the Middle Jurassic, is associated with northward subduction of the Bangong–Nujiang Ocean. The second deformation event, accommodated by northeast-striking faults, occurred during the Early Cretaceous and is interpreted as resulting from far-field oblique flat-slab subduction of the Paleo-Pacific Plate. Reactivation of these northeast-striking faults during the Eocene is associated with the thrusting of the Longmenshan belt. The final deformation event, dating to the Oligocene, is attributed to the eastern expansion of the Tibetan Plateau and the subsequent counterclockwise rotation of the Sichuan Basin.

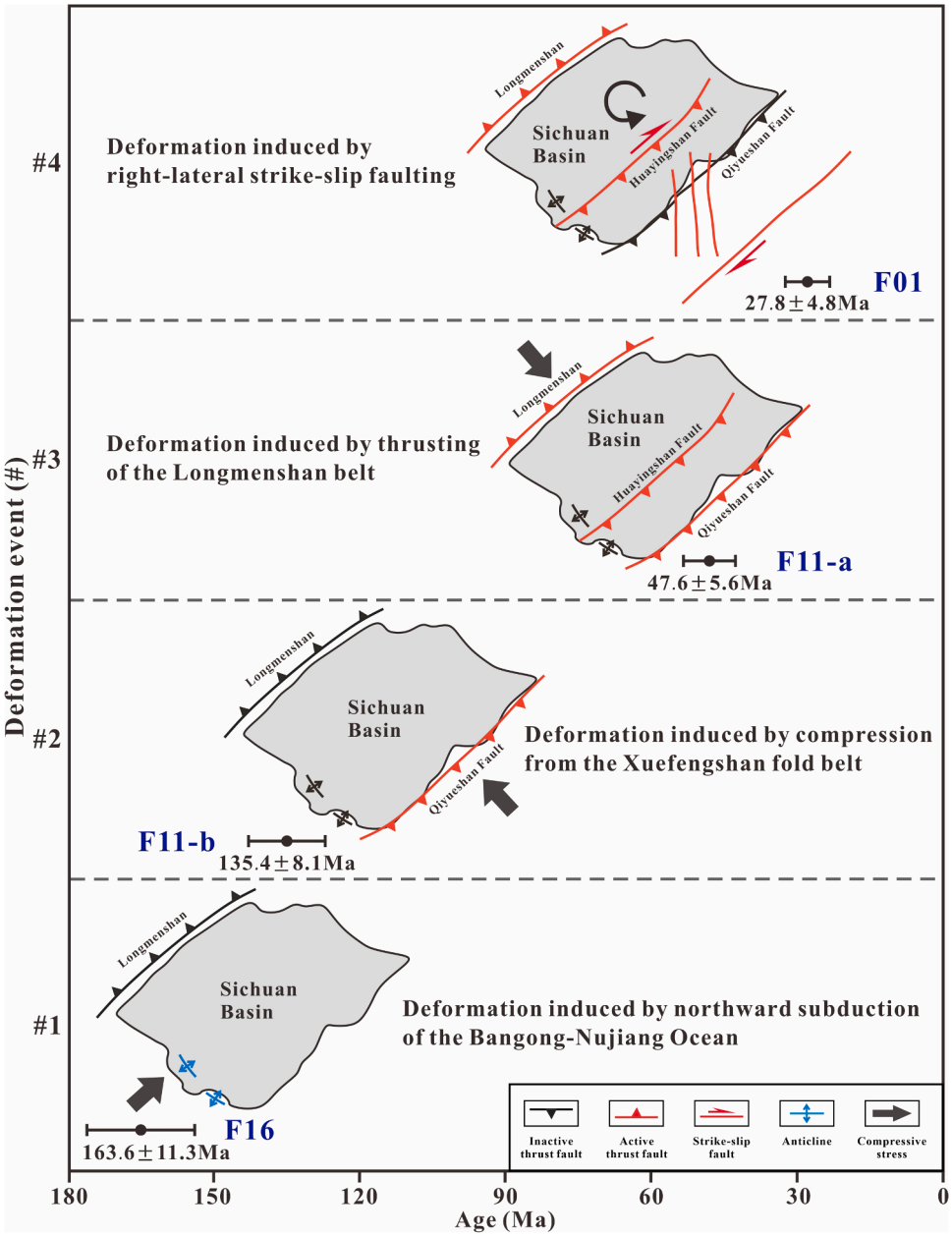

Fig. 6. Summary of four dated deformation events in the eastern Sichuan Basin, with the corresponding calcite U-Pb ages (±2σ errors).

CRediT authorship contribution statement

Lianbo Zeng: Project administration, Funding acquisition, Conceptualization. **Liang Luo:** Writing – review & editing, Writing – original draft, Validation, Methodology, Investigation, Formal analysis, Conceptualization. **Xuan Yang:** Visualization, Investigation. **Yangfan Zhou:** Visualization, Investigation.

Declaration of Competing Interest

The authors declare that they have no known competing financial interests or personal relationships that could have appeared to influence the work reported in this paper.

Acknowledgments

The financial support by the National Natural Science Foundation of China (No. U21B2062) is greatly appreciated.

Data availability

The data that has been used is confidential.

References

Amidon, W.H., Kylander-Clark, A.R., Barr, M.N., Graf, S.F., West, Jr, D.P., 2022. Pace of passive margin tectonism revealed by U-Pb dating of fracture-filling calcite. Nat. Commun. 13 (1), 1953.

Ault, A.K., Gautheron, C., King, G.E., 2019. Innovations in (U–Th)/He, fission track, and trapped charge thermochronometry with applications to earthquakes, weathering, surface-mantle connections, and the growth and decay of mountains. Tectonics 38 (11), 3705–3739.

Bilau, A., Bienveignant, D., Rolland, Y., Schwartz, S., Godeau, N., Guihou, A., Deschamps, P., Mangenot, X., Brigaud, B., Boschetti, L., Dumont, T., 2023a. The Tertiary structuration of the Western Subalpine foreland deciphered by calcite-filled faults and veins. EarthSci. Rev. 236, 104270.

Bilau, A., Rolland, Y., Dumont, T., Schwartz, S., Godeau, N., Guihou, A., Deschamps, P., 2023b. Early onset of Pyrenean collision (97–90 Ma) evidenced by U–Pb dating on calcite (Provence, SE France). Terra Nova 35 (5), 413–423.

Bilau, A., Rolland, Y., Schwartz, S., Godeau, N., Guihou, A., Deschamps, P., Brigaud, B., Noret, A., Dumont, T., Gautheron, C., 2021. Extensional reactivation of the Penninic

Frontal Thrust 3 Ma ago as evidenced by U-Pb dating on calcite in fault zone cataclasite. Solid Earth 12, 237–251.
Cao, Y., Xu, Q., Zheng, J., Tan, X., Li, M., Kershaw, S., Li, L., Qiu, Y., Deng, W., 2023. Two stages of Late Cretaceous to Neogene deformation of the Huayingshan tectonic belt, eastern Sichuan Basin, SW China. J. Asian Earth Sci., 105779
Champagnac, J.D., Molnar, P., Anderson, R.S., Sue, C., Delacou, B., 2007. Quaternary erosion-induced isostatic rebound in the western Alps. Geology 35 (3), 195–198.
Deng, B., Liu, S.G., Li, Z.W., Jansa, L.F., Liu, S., Wang, G.Z., Sun, W., 2013. Differential exhumation at eastern margin of the Tibetan Plateau, from apatite fission-track thermochronology. Tectonophysics 591, 98–115.
Dilek, Y., Tang, L., 2021. Magmatic record of the Mesozoic geology of Hainan Island and its implications for the Mesozoic tectonomagmatic evolution of SE China: effects of slab geometry and dynamics in continental tectonics. Geol. Mag. 158 (1), 118–142.
Dong, S.W., Zhang, Y.Q., Gao, R., Su, J.B., Liu, M., Li, J.H., 2015. A possible buried Paleoproterozoic collisional orogen beneath central South China: evidence from seismic-reflection profiling. Precambrian Res 264, 1–10.
Enkin, R., Yang, Z., Chen, Y., Courtillot, V., 1992. Paleomagnetic constraints on the geodynamic history of the major blocks of China from the Permian to the present. J. Geophys. Res. Solid Earth 97 (B10), 13953–13989.
Faure, M., Lin, W., Le Breton, N., 2001. Where is the North China-South China block boundary in eastern China? Geology 29 (2), 119–122.
Feng, Q., Qiu, N., Wu, H., Koyi, H., 2023. Thermo-kinematic constraints on restoration of the Eastern Sichuan fold-and-thrust belt, South China. Tectonics 42 (9), e2022TC007630.
Feng, W., Wang, F., Guan, J., Zhou, J., Wei, F., Dong, W., Xu, Y., 2018. Geologic structure controls on initial productions of lower Silurian Longmaxi shale in south China. Mar. Petrol. Geol. 91, 163–178.
Gu, Z., Wang, X., Nunns, A., Zhang, B., Jiang, H., Fu, L., Zhai, X., 2021. Structural styles and evolution of a thin-skinned fold-and-thrust belt with multiple detachments in the eastern Sichuan Basin, South China. J. Struct. Geol. 142, 104191.
He, W., Zhou, J., 2018. Analogue modeling of feature and formation mechanism of horsetail-shaped fold belt in Southeast Sichuan Basin, South China. Earth Sci. 43 (6), 2133–2148.
Hou, Z.Q., Liu, L, J., Zhang, H.J., Xu, B., Wang, Q.F., Yang, T.N., Wang, R., Zheng, Y.C., Li, Y.C., Gao, L., Yu, N., Wang, X.L., Miao, Z., Han, S.C., Lv, Q.T., 2024. Cenozoic eastward growth of the Tibetan Plateau controlled by tearing of the Indian slab. Nat. Geosci. 17, 255–263.
Hu, Z., Zhu, G., Liu, G., Zhang, B., 2009. The folding time of the Eastern Sichuan jura-type fold belt: evidence from unconformity. Geol. Rev. 55 (1), 32–42.
Jia, D., Li, Y.Q., Yan, B., Li, Z.G., Wang, M.M., Chen, Z.X., Zhang, Y., 2020. The Cenozoic thrusting sequence of the Longmen Shan fold-and-thrust belt, eastern margin of the Tibetan plateau: insights from low-temperature thermochronology. J. Asian Earth Sci. 198, 104381.
Jullien-Sicre, A., Missenard, Y., Blaise, T., Augier, R., Parizot, O., Haurine, F., 2025. Timing of contractional stress propagation, from the Pyrenean orogen to the intraplate domain, evidenced by U-Pb dating of syn-kinematic calcite. Tectonics 44 (2), e2024TC008634.
Li, C., He, D., Lu, G., Wen, K., Simon, A., Sun, Y., 2021. Multiple thrust detachments and their implications for hydrocarbon accumulation in the northeastern Sichuan Basin, southwestern China. AAPG (Am. Assoc. Pet. Geol.) Bull. 105, 357–390.
Li, C., He, D., Sun, Y., He, J., Jiang, Z., 2015. Structural characteristic and origin of intra-continental fold belt in the eastern Sichuan basin, South China Block. J. Asian Earth Sci. 111, 206–221.
Li, J., Dong, S., Cawood, P.A., Zhao, G., Johnston, S.T., Zhang, Y., Xin, Y., 2018. An Andean-type retro-arc foreland system beneath northwest South China revealed by SINOPROBE profiling. Earth Planet Sci. Lett. 490, 170–179.
Li, J., Zhang, Y., Dong, S., Johnston, S.T., 2014. Cretaceous tectonic evolution of South China: a preliminary synthesis. Earth Sci. Rev. 134, 98–136.
Li, S., Li, Y., He, Z., Chen, K., Zhou, Y., Yan, D., 2020. Differential deformation on two sides of Qiyueshan fault along the eastern margin of Sichuan Basin, China, and its influence on shale gas preservation. Mar. Pet. Geol. 121, 104602.
Li, Z., Li, X., 2007. Formation of the 1300-km-wide intracontinental orogen and postorogenic magmatic province in Mesozoic South China: a flat-slab subduction model. Geology 35 (2), 179–182.
Liu, S., Qian, T., Li, W., Dou, G., Wu, P., 2015. Oblique closure of the northeastern Paleo-Tethys in central China. Tectonics 34 (3), 413–434.
Liu, Y., Li, S., Yu, S., Cao, X., Zhou, J., Li, Y., Wang, Y.H., Xu, L., Guo, R., Zhou, Z., 2019. The Mesozoic collage and orogeny process of micro-blocks in Bangong-Nujiang suture zone, Tibetan Plateau. Geotecton. Et. Metallog. 43 (4), 824–838.
Ludwig, K.R., 2012. User's manual for Isoplot 3.75. A geochonological toolkit for microsoft excel. Berkeley Geochronol. Cent. Spec. Publ. v. 5, 1–75.
Mei, L., Liu, Z., Tang, J., Shen, C., Fan, Y., 2010. Mesozoic intra-continental progressive deformation in western Hunan-Hubei-eastern Sichuan provinces of China: evidence from apatite fission track and balanced cross-section. Earth Sci. J. China Univ. Geosci. 35 (2), 161–174.
Meng, Q., Zhang, G., 2000. Geologic framework and tectonic evolution of the Qinling orogen, central China. Tectonophysics 323 (3–4), 183–196.
Mouthereau, F., Boschetti, L., Larrey, M., Brichau, S., Beaudoin, N.E., Huyghe, D., Roberts, N., Daëron, M., 2025. Tracking lithospheric delamination and surface processes across the Messinian salinity crisis. Nat. Commun. 16 (1), 1–13.
Northrup, C., Royden, L., Burchfiel, B., 1995. Motion of the Pacific plate relative to Eurasia and its potential relation to Cenozoic extension along the eastern margin of Eurasia. Geology 23 (8), 719–722.
Nuriel, P., Craddock, J., Kylander-Clark, A., Uysal, I., Weinberger, R., 2019. Reactivation history of the North Anatolian fault zone based on calcite age-strain analyses. Geology 47 (5), 465–469.
Nuriel, P., Weinberger, R., Kylander-Clark, A., Hacker, B., Craddock, J., 2017. The onset of the Dead Sea transform based on calcite age-strain analyses. Geology 45 (7), 587–590.
Paton, C., Hellstrom, J., Paul, B., Woodhead, J., Hergt, J., 2011. Iolite: Freeware for the visualisation and processing of mass spectrometric data. J. Anal. At. Spectrom. 26, 2508.
Qiu, N., Feng, Q., Tenger, B., Shen, B., Ma, Z., Yu, L., Cao, A., 2020. Yanshanian-Himalayan differential tectono-thermal evolution and shale gas preservation in Dingshan area, southeastern Sichuan Basin. Acta Pet. Sin. 41 (12), 1610.
Ring, U., Gerdes, A., 2016. Kinematics of the Alpenrhein-Bodensee graben system in the Central Alps: oligocene/miocene transtension due to formation of the Western Alps arc. Tectonics 35 (6), 1367–1391.
Roberts, N., Holdsworth, R., 2022. Timescales of faulting through calcite geochronology: a review. J. Struct. Geol. 158, 104578.
Roberts, N., Walker, R., 2016. U-Pb geochronology of calcite-mineralized faults: absolute timing of rift-related fault events on the northeast Atlantic margin. Geology 44 (7), 531–534.
Royden, L.H., Burchfiel, B.C., Hilst, R., 2008. The geological evolution of the Tibetan Plateau. Science 321, 1054–1058.
Shen, C., Mei, L., Xu, S., 2009. Fission track dating of Mesozoic sandstones and its tectonic significance in the Eastern Sichuan Basin, China. Radiat. Meas. 44 (9–10), 945–949.
Shi, H., Shi, X., Glasmacher, U.A., Yang, X., Stockli, D.F., 2016. The evolution of eastern Sichuan basin, Yangtze block since Cretaceous: constraints from low temperature thermochronology. J. Asian Earth Sci. 116, 208–221.
Tapponnier, P., 2001. Oblique stepwise rise and growth of the Tibet Plateau. Science 294, 1671–1677.
Tian, Y., Kohn, B.P., Qiu, N., Yuan, Y., Hu, S., Gleadow, A.J.W., Zhang, P., 2018. Eocene to miocene out-of-sequence deformation in the Eastern Tibetan plateau: insights from shortening structures in the Sichuan Basin. J. Geophys. Res. Solid Earth 123, 1840–1855.
Wang, E., Kai, M., Zhe, S., Meng, Q., Chu, J., Chen, Z., Gang, W., Shi, X., Liang, X., 2014. Block rotation: Tectonic response of the Sichuan basin to the southeastward growth of the Tibetan Plateau along the Xianshuihe-Xiaojiang fault. Tectonics 33 (5), 686–718.
Wang, G., Zhang, W., Zhou, X., Jia, J., Yu, H., 2008. Middle Jurassic high-pressure shearing reveled by phengite in Jiayuqiao metamorphic complex, eastern Tibet. Acta Petrol. Sin. 24 (2), 395–400.
Wang, Z., Zhang, J., Tao, L.I., Xie, G., Zongjin, M.A., 2010. Structural analysis of the multi-layer detachment folding in Eastern Sichuan province. Acta Geol. Sin. 84, 497–514.
Wu, S.T., Wang, Y.P., Xu, C.X., 2015. Research progress on reference materials for in situ elemental analysis by laser ablation-inductively coupled plasma-Mass spectrometry. Rock. Miner. Anal. 34 (5), 503–511.
Xu, W.Q., Yin, H.W., Zhao, S.X., Zhang, C.L., Li, B., Jia, D., Li, C.S., Wang, W., 2024. Influence of multiple detachments on structural vergence and evolution of the thin-skinned fold-and-thrust belt in the eastern Sichuan Basin: Insights from numerical modeling. J. Struct. Geol. 180, 105068.
Yan, D.P., Zhou, M.F., Song, H.L., Wang, X.W., Malpas, J., 2003. Origin and tectonic significance of a mesozoic multi-layer over-thrust system within the Yangtze block (south China). Tectonophysics 361, 239–254.
Yang, Y., Wen, L., Luo, B., Song, J., Chen, X., Wang, X., Hong, H., Zhou, G., He, Q., Zhang, X., Zhong, J., Liu, R., Shan, S., 2016. Sedimentary tectonic evolution and reservoir-forming conditions of the Dazhou–Kaijiang paleo-uplift, Sichuan Basin. Nat. Gas. Ind. B 3, 515–525.
Yin, A., 2010. Cenozoic tectonic evolution of Asia: a preliminary synthesis. Tectonophysics 488 (1–4), 293–325.
Zhang, Y.Q., Qiu, E.K., Dong, S.W., Li, J.H., Shi, W., 2022. Late Mesozoic intracontinental deformation and magmatism in North and NE China in response to multi-plate convergence in NE Asia: an overview and new view. Tectonophysics 835, 229377.
Zhong, Y., Hu, X., Liu, W., Xia, B., Zhang, X., Huang, W., Fu, Y., Wang, Y., 2018. Age and nature of the jurassic-early cretaceous mafic and ultramafic rocks from the Yilashan area, Bangong-Nujiang suture zone, central Tibet: implications for petrogenesis and tectonic evolution. Int. Geol. Rev. 60 (10), 1244–1266.
Zhu, C., Qiu, N., Liu, Y., Xiao, Y., Hu, S., Chen, Z.Q., 2019. Constraining the denudation process in the eastern Sichuan Basin, China using low-temperature thermochronology and vitrinite reflectance data. Geol. J. 54, 426–437.